METAMATERIALS

Demonstration of a third-order hierarchy of topological states in a three-dimensional acoustic metamaterial

Matthew Weiner^{1,2}, Xiang Ni^{1,2,3}, Mengyao Li^{1,2}, Andrea Alù^{1,2,3}*, Alexander B. Khanikaev^{1,2}*

Classical wave systems have constituted an excellent platform for emulating complex quantum phenomena, such as demonstrating topological phenomena in photonics and acoustics. Recently, a new class of topological states localized in more than one dimension of a *D*-dimensional system, referred to as higher-order topological (HOT) states, has been reported, offering an even more versatile platform to confine and control classical radiation and mechanical motion. Here, we design and experimentally study a 3D topological acoustic metamaterial supporting third-order (0D) topological corner states along with second-order (1D) edge states and first-order (2D) surface states within the same topological bandgap, thus establishing a full hierarchy of nontrivial bulk polarization–induced states in three dimensions. The assembled 3D topological metamaterial represents the acoustic analog of a pyrochlore lattice made of interconnected molecules, and is shown to exhibit topological bulk polarization, leading to the emergence of boundary states.

Copyright © 2020
The Authors, some rights reserved; exclusive licensee American Association for the Advancement of Science. No claim to original U.S. Government Works. Distributed under a Creative Commons Attribution NonCommercial License 4.0 (CC BY-NC).

INTRODUCTION

Topological acoustics and mechanics have been explored as a powerful platform for the implementation of a plethora of topological phenomena (1-4). A bias for sound propagation imparted by the angular momentum carried by a rotating fluid or by rotational motion in mechanical resonators has been used to emulate the effect of magnetic bias and to demonstrate the emergence of quantum Hall effect (QHE)-like states with robust edge transport for acoustics and mechanics (5-11). In parallel, a variety of symmetry-protected topological acoustic states have been reported, including Zak phase in one-dimensional (1D) acoustic lattices (12), quantum spin Hall effect (QSHE) (13-16), and nontrivial bulk polarization-induced edge and corner states in 2D Kagome lattices (17-20). More recently, versatile 3D structures fabricated by either direct assembly or advanced 3D manufacturing have been used to demonstrate Weyl points and Fermi arc-like surface states in 3D acoustic and mechanical metamaterials (21-24), as well as mechanical quadrupolar topological insulators (25-27). 3D geometries markedly expand the design opportunities for acoustic topological metamaterials, thus offering the possibility of demonstration of unprecedented topological phenomena, often still unobserved in their condensed matter or photonic analogs. Wannier-type higher-order topological (HOT) insulators with a hierarchy of states represent one example in which the system dimensionality becomes crucial. These states have so far been demonstrated only in 2D topological systems, being limited therefore to second-order states (17, 19, 20, 28). Higher-order hierarchies of topological states have so far evaded experimental observation. In this work, we experimentally observe for the first time such hierarchy of second- and third-order states in a 3D acoustic metamaterial. We exploit 3D printing and a snap assembly technique to construct an acoustic analog of the topological pyrochlore lattice, which hosts a third-order hierarchy of topological states. We show

RESULTS

Topological acoustic metamaterial design

A 3D acoustic metamaterial emulator of the pyrochlore lattice (28, 30) is realized using metamolecules (unit cells) schematically shown in Fig. 1 (A and B), whose specific dimensions are given in Materials and Methods. Each molecule consists of four acoustic resonators, with acoustic pressure modes oscillating along the axial direction, as shown in the inset to Fig. 1A. We choose to work with the fundamental mode, whose only node appears in the center of the individual cavity of the resonator. To form the lattice, the resonators are coupled through narrow cylindrical channels whose position on the resonator is carefully chosen to respect the crystalline symmetries of the pyrochlore lattice. The control over coupling between resonators within and between adjacent metamolecules of the metacrystal, which is required to induce bulk topological polarization, is achieved by varying the diameter of the cylindrical coupling channels. Because the acoustic modes are strongly bound to the resonant cavities and the design of the structure only allows nearest neighbor coupling, the tight-binding model (TBM) can be an effective modeling tool for our system, with nearest-neighbor hopping described by intra-cell κ and inter-cell γ coupling parameters. An analytical construction of the Hamiltonian is presented in section S1. COMSOL Multiphysics (acoustic module) has been used to verify the results with full-wave finite element method (FEM) simulations. If the diameter of the intraconnected channels is smaller than the one of the interconnected channels, $\kappa < \gamma$, then the structure is referred to as the "expanded" crystal, implying stronger coupling among resonators of the adjacent metamolecules. In the opposite condition, $\kappa > \gamma$, the structure is "shrunken," and modes

that the manufactured acoustic metacrystal has topological bulk polarization, and we experimentally demonstrate a hierarchy of Wannier-type HOT states in three dimensions by observing in the same sample first-order surface, second-order edge, and third-order corner states localized in one, two, and three dimensions, respectively. The presence of this rich hierarchy of topological phase-induced states paves the way to a whole host of applications (29) because they exhibit resilience to disorder as long as the structure remains adiabatically connected to the nontrivial topological phase.

¹Department of Electrical Engineering, Grove School of Engineering, City College of the City University of New York, 140th Street and Convent Avenue, New York, NY 10031, USA. ²Physics Program, Graduate Center of the City University of New York, New York, NY 10016, USA. ³Photonics Initiative, Advanced Science Research Center, City University of New York, New York, NY 10031, USA.

^{*}Corresponding author. Email: aalu@gc.cuny.edu (A.A.); akhanikaev@ccny.cuny.edu (A.B.K.)

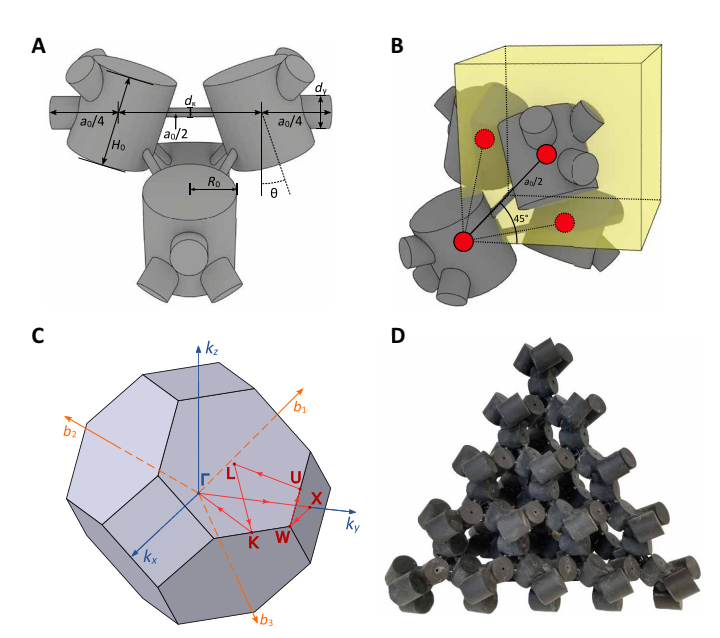


Fig. 1. Concept and design of the acoustic pyrochlore lattice. (A) Schematic and realistic design of the Wigner-Seitz unit cell of the expanded pyrochlore lattice. (B) Schematic of the Wigner-Seitz unit cell inserted into the fcc lattice structure. (C) First Brillouin zone of the fcc lattice, with labeled high symmetry points, high symmetry paths, and reciprocal lattice vectors. (D) Photograph of the 3D topological metamaterial assembled from 3D printed metamolecules, with boundary cells attached. Each side length of the crystal consists of four metamolecules (12 acoustic resonators). Photo credit: Zachary Talis, Rochester Institute of Technology. The inset in (A) shows the field profile of axial dipolar mode of single resonator. The inset in (D) features an example of boundary cell with an inner cavity of shorter (90%) axial height than the rest of the structure (see Materials and Methods for details).

are strongly coupled within the resonators of the metamolecule within the same unit cell. The acoustic resonators in the metamaterial are aligned to show the sites and primitive vectors of the face-centered cubic (fcc) lattice in Fig. 1B and the corresponding first Brillouin zone shown in Fig. 1C. As the dimensions of the crystal exceeded the print volume of currently available stereolithography (SLA) 3D printers, the hybrid approach, combining 3D printing of the constitutive elements and subsequent snap assembly, was used. The metamolecules were 3D printed and snapped together using the interlocking features that are deliberately introduced in the design, thus allowing the assembly of rigid and stable large-scale metacrystals. The assembled finite structure consisting of 20 metamolecules (80 resonators) is shown in Fig. 1D. Note that the boundaries of the crystal are terminated by smaller resonators, which are designed to have resonant frequencies detuned from the spectral region of interest to high frequency range, yielding an effective boundary condition analogous to the terminated boundary in TBM. These are required to preserve the Γ_4 generalized chiral symmetry present in the pyrochlore structure with nearest neighbor coupling (section S3) (20).

Nontrivial topology and bulk polarization

First, we theoretically explore the band structure of the unit cell, as shown in Fig. 2 (A and B). In the ideal pyrochlore lattice, with $\kappa=\gamma$ (Fig. 2A), a line of degeneracy along the X-W high symmetry path can be observed. The degeneracy of this line is broken by making the inter-cell and intra-cell couplings different, $\kappa\neq\gamma$ (Fig. 2B). Through both semi-analytical TBM and the first-principles FEM modeling of

the structure, we observe band inversion at the W point between two cases of expanded and shrunken crystals, which indicates a nontrivial topological transition. However, energy bands alone are not sufficient to determine the topological difference between expanded and shrunken crystals, and further analysis of the associated eigenstates is required.

To explicitly confirm the topological phase transition between expanded and shrunken crystals, we calculated the bulk topological polarization using the eigenvalue problem of the Wilson loops (31). The bulk polarization of the lowest energy band, defining the emergence of Wannier-type HOT states in the first bandgap above this band for both cases of the expanded and shrunken lattices, can be obtained through the Wannier band $v_3(k_1, k_2)$, where (k_1, k_2) vary along the reciprocal lattice vectors $\mathbf{b_1}$, $\mathbf{b_2}$ in momentum space, and the Wilson loop is evaluated along the direction of the reciprocal lattice vector $\mathbf{b_3}$ (Fig. 1C). Then, the bulk polarization of the lowest energy band of interest is defined as

$$p_3(k_1, k_2) = \frac{1}{N_1 N_2} \sum_{\mathbf{b}_3} v_3(k_1, k_2)$$
 (1)

where $N_{1,2}$ is the total number of points in the discretized momentum space. Because of the spatial symmetries of the pyrochlore crystal, the bulk polarizations with cyclically permutated indexes are equivalent to each other, and therefore, the system is characterized by nontrivial bulk polarization in all three dimensions. As shown in Fig. 2 (C and D), the bulk polarization of the expanded crystal calculated through Eq. 1 yields ¹/₄, which indicates that the average position of the modes belonging to the lowest energy band has a $\frac{a_0}{4}$ deviation (shift) from the center of the sites in the unit cell. According to the bulk-boundary correspondence principle, when boundaries are introduced in the expanded pyrochlore lattice with nonvanishing bulk polarization, the boundary modes such as surface, edge, and corner states should appear hanging at the dangling sites of the corresponding terminations of the crystal. Meanwhile, the bulk polarization of the shrunken crystal is zero, implying that the average position of the desired modes resides at the center of the four sites in the metamolecule, and no boundary modes are present at any boundary (section S4).

Experimental demonstration of a hierarchy of Wannier-type HOT states

We numerically calculated the energy spectrum of the metamaterial sample in Fig. 1D as a function of the ratio κ/γ (Fig. 3A) by using TBM of the finite crystal. Based on the prediction from nontrivial bulk polarization outlined in the previous section, for the case of expanded lattice (when $\frac{\kappa}{\gamma}$ < 1), we expect surface (purple-colored), edge (blue-colored), and corner modes (red-colored) to emerge at the boundaries. Both TBM and numerical simulations based on FEM fully confirm these predictions. When $\frac{\kappa}{\nu} < \frac{1}{3}$, fourfold degeneracy corner modes split from the bulk continuum (yellow-colored bands) and, as can be proven analytically (see the Supplementary Materials for details), the transition point occurs at $\frac{\kappa}{\gamma} = \frac{1}{3}$. In the 3D printed structure fabricated for our experimental investigation, we choose to work in the $\kappa/\gamma = 0.111$ regime of the energy spectrum of the lattice (indicated by dashed lines in Fig. 3A). In this case, the zero-energy corner states, as well as the edge and surface states, appear fully immersed into the bulk bandgap and show no overlap with the bulk continuum. In agreement with the TBM energy spectrum, the frequency response spectra of different sites extracted from

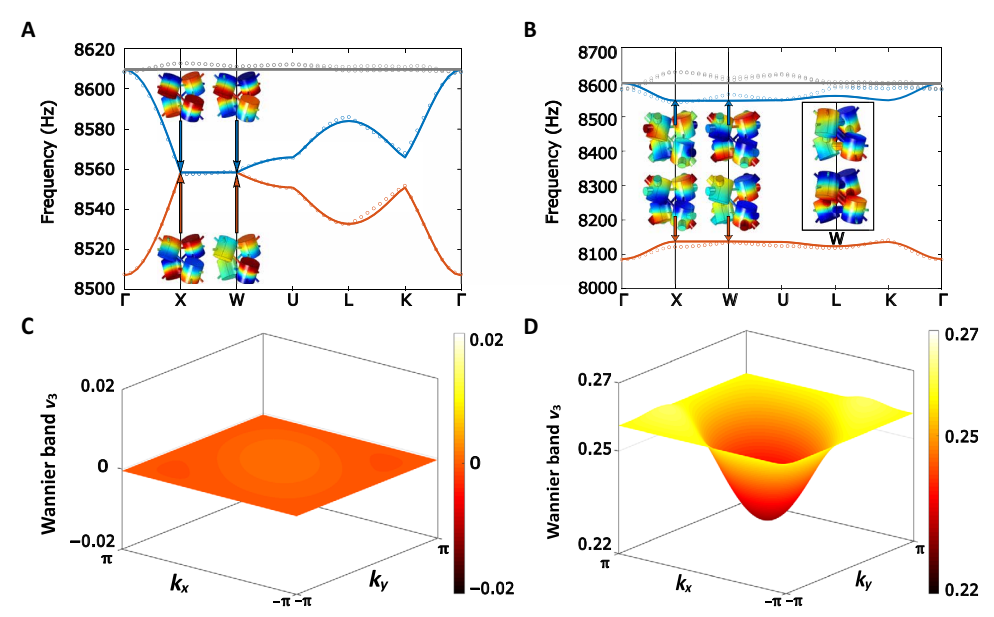


Fig. 2. Theoretical prediction of nontrivial bulk polarization. (A) Dispersion relation of the undimerized and (B) dimerized (expanded or shrunken) unit cell obtained by TBM (solid lines) and first-principles COMSOL calculations (circular dots) along a high symmetry path through the Brillouin zone shown in Fig. 1C and the corresponding mode profiles shown at X and W points. The inset in (B) shows the mode profiles of the shrunken unit cell at X and W, demonstrating the characteristic band inversion of topological systems. (C and D) Wannier bands of the pyrochlore lattice obtained by TBM for (C) the shrunken and (D) expanded unit cell. The ratio of intra-cell and inter-cell hopping terms are $\kappa/\gamma = 0.111$ and $\kappa/\gamma = 9.009$ for the expanded and shrunken cases, respectively.

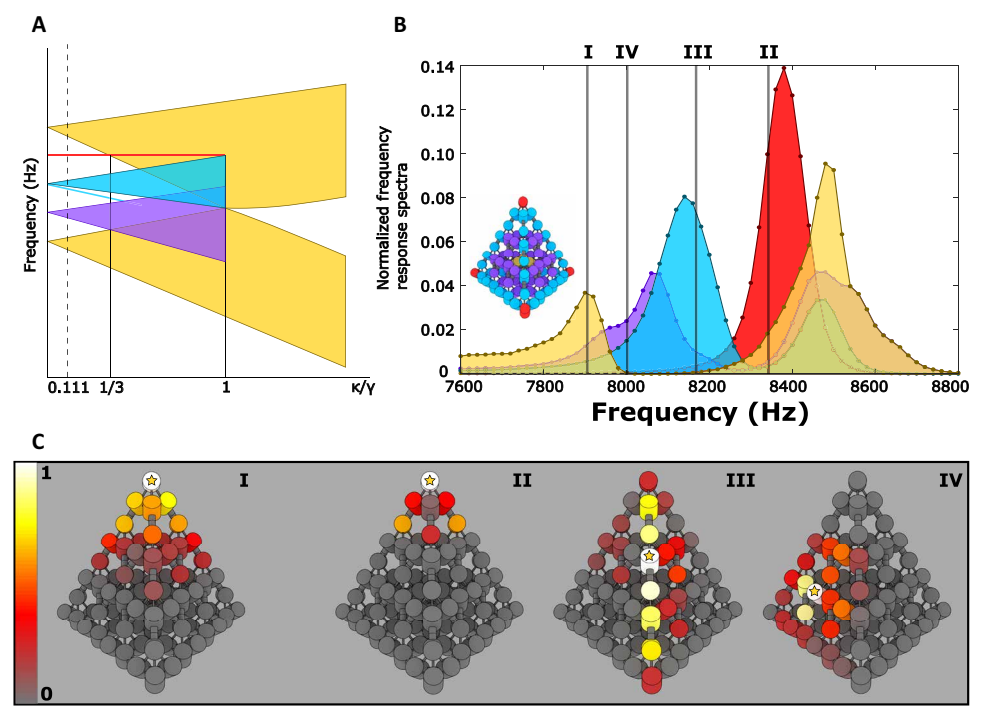


Fig. 3. Experimental demonstration of second- and third-order topological edge and corner states. (A) Energy spectrum obtained from TBM for the pyrochlore lattice. Yellow-, purple-, blue-, and red-colored shaded regions are for bulk, surface, edge, and corner states, respectively. (B) Normalized density of states for the expanded lattice obtained from the measurements of the frequency response at the top of each site. Each region's densities of states (bulk, surface, edge, and corner) were obtained by filter functions of bulk, surface, edge, and corner, respectively. The full width at half maximum of the corner state is approximately 140 Hz with a maximum at 8380 Hz, corresponding to a quality factor of 60, well within the estimate for an individual resonator to permit the topological properties of this mode. (C) Logarithmic map of the spatial distribution without filter functions of acoustic power with source placed at the starred cylinder and measured at frequencies I, II, III, and IV in (B).

acoustic measurements on the structure (Fig. 3B) reveal a wide bulk bandgap with lower and upper bulk bands, as well as a hierarchy of topological boundary modes, including surface states, edge states, and (fourfold degenerate) corner states (localized at the four corners of the structure). In contrast to the lower bulk band, the upper bulk band also shows up the spectra for surface and edge sites. This observation is related to the fact that the modes of the upper bulk band penetrate into the surface and edge resonators, as opposed to the lower band, where the topological polarization removes the corresponding surface and edge degrees of freedom from the bulk eigenmodes. Materials and Methods provides details of the procedure to extract the frequency response spectra for different regions from experimental measurements. The corner states appear at "zero-energy," i.e., their frequency corresponds to the frequency of a separate individual resonator; however, the collective nature of these modes is evidenced by the nonvanishing field strength in other sites of the lattice. All the topological states appear within the bulk bandgap, with some overlap due to the finite bandwidth of the corresponding spectral lines caused by their finite lifetime. Some overlap among the bulk, surface, edge, and corner spectra can be seen in Fig. 3B and is attributed to inhomogeneous broadening due to energy dissipation. Two major loss mechanisms in our experiment are (i) the absorption in the resin used in 3D printing and (ii) the leakage through the probe holes, which are deliberately introduced in the design of the individual resonators to allow excitation and probing of the acoustic field. The resultant experimentally measured quality factors of the individual resonators are within the range of 50 to 60, and therefore, the corresponding finite lifetimes of the modes of the lattice are long enough not to alter their topological nature, making them clearly observable in our system. To validate our findings and highlight the topological nature of the observed states, we also fabricated a trivial shrunken structure, which was found to host bulk modes only, further evidencing the topological origin of the observed surface, edge, and corner states. The frequency response spectra for the shrunken structure are shown in section S4. In this scenario, the spectra for surface, edge, and corner sites all appear in the lower bulk band as well, thus confirming that the topological polarization is trivial and the wavefunction of the bulk modes penetrates into boundary sites (section S4 and fig. S2). This is an important distinction from the nontrivial case, when these sites are excluded from the wavefunction of the lower bulk band due to the topological bulk polarization of the lower bulk band as in Fig. 3B.

The experimentally measured field profiles of all the modes, shown in Fig. 3C, are in excellent agreement with the numerically calculated profiles of Wannier-type higher order states. From Fig. 3C, one can easily ascertain the difference between field profiles of the exponentially decaying bulk modes (excited at the frequency within the bulk band indexed by label I in Fig. 3B) and of the extremely localized zero-energy corner state excited at the corresponding frequency (indexed by label II in Fig. 3B). Note that the field decay of the bulk modes is less rapid, following a $1/r^2$ dependence with an exponential correction due to loss. It is worth mentioning that the generalized chiral symmetry in the pyrochlore lattice provides inherent robustness of the corner modes, as the corner states are always pinned to zero-energy states, and their field profiles are ideally localized at one of the sublattices, which is evident in the corner mode spectral profile in Fig. 3C. The generalized chiral symmetry for the present case of 3D pyrochlore lattice is described by the operator $\hat{\Gamma}_4$, with the property $\hat{\Gamma}_4^4 = I$, connecting a sequence of inequivalent Hamiltonians \widehat{H}_n with the same spectrum $\widehat{\Gamma}^n \widehat{H}_0 \widehat{\Gamma}^{-n} = \widehat{H}_n$, where n=1,2,3, and $H_0+H_1+H_2+H_3=0$ (section S3). As can be seen from the logarithmic field maps in Fig. 3C (right), the corner state predominantly localizes on the same sublattice. Thus, the acoustic pressure amplitude at the atoms of different sublattices within the same unit cell appears to be at least 500 times smaller compared to the amplitude in the same sublattice of the adjacent cells (only 40 times weaker due to the exponential localization of the states). As expected, the sublattice localization is not observed for the bulk modes plotted in the left panel of Fig. 3C.

In addition to corner states localized in three dimensions, the nonzero value of bulk topological polarization gives rise to the formation of another class of Wannier-type higher-order states-second-order edge states confined to the edges and first-order surface states confined to the surface of the fabricated finite metacrystal. These modes are also shown in Fig. 3C, where we can see that they exhibit extreme localization to a particular edge or surface, respectively. For the edge mode, the mode is excited halfway between the terminating corners, and it forms a standing wave-like profile with two nodes located at the respective corners. For the surface mode, the mode is excited in the inner part of the surface at the starred site, where it also forms a membrane-like standing wave profile with fixed constraint boundary conditions located along the edges.

DISCUSSION

Advanced manufacturing techniques based on 3D printing metamolecules and their snap assembly to form complex acoustic metamaterials provides exciting opportunities in acoustics. Here, this platform has been applied to fabricate a 3D topological metamaterial forming the acoustic analog of pyrochlore crystal and supporting a regime with nontrivial topological bulk polarization. We demonstrated for the first time that this topological polarization leads to the emergence of a hierarchy of Wannier-type HOT states, third order states confined to corners, second-order states localized at the edges, and first-order states localized at the surface of the 3D metacrystal. The respective modes show strong and topologically robust confinement to the respective edges and corners, making them ideal candidates for applications in which precise control of energy localization is critical. In this respect, topological metamaterials not only hold the promise for desirable field concentration but also add the unique feature of robustness, which ensures the spectral position of the HOT states to be stable, as long as the generalized chiral symmetry of the manufactured structure is ensured by its design and fabrication. The use of additional synthetic degrees of freedom, engineered by the complex geometries of the 3D multimodal metamolecules (24), may further facilitate control of topological acoustic modes, opening even more interesting applications, with sound waves filtered, steered, and routed based on their internal synthetic polarization.

MATERIALS AND METHODS

Experimental design

The unit cell designs of the topological expanded lattice are shown in Fig. 1 (A and B) with lattice constant $a_0 = 61.66$ mm, height $H_0 = 20.00$ mm, and radius $r_0 = 9.70$ mm. The connectors between the cylinders are radial channels with diameter $d_{\gamma} = 3.66$ mm and $d_{\kappa} = 1.00$ mm. To preserve the rotational symmetries of the pyrochloric

unit cell, we rotated the cylinders about their axis along the z direction by angle $\theta=18.60^\circ$ in the y-z plane (such that the three modes remain degenerate at Γ point, as shown in Fig. 2B). In addition, these structures are optimized for the single-mode fundamental harmonic of the individual cavity resonator such that there are no other internal degrees of freedom within the unit cell within the frequency range of interest. The centers of the four cylinders in each unit cell are aligned to form the fcc lattice. The boundary cells, as shown in the photograph of the finite structure (Fig. 1D), have the same geometric parameters except their heights are 90% that of the cylinders within the unit cell.

The unit cells and boundary cells were fabricated using the B9Creator v1.2 3D printer. All cells were made with acrylic-based light-activated resin, a type of plastic that hardens when exposed to ultraviolet light. Each cell was printed with a sufficient thickness to ensure a hard wall boundary condition, and narrow probe channels were intentionally introduced on top and bottom of each cylinders to excite and measure local pressure amplitude at each site. The diameter of each port is 2.50 mm with a height of 2.20 mm. When not in use, the probe channels were sealed with plumber's putty. Each unit cell and boundary cell were printed one at a time, and the models were designed specifically to interlock tightly with each other. The expanded structure shown in Fig. 1D contains 20 unit cells and 60 boundary cells. For all measurements, a frequency generator and fast Fourier transform (FFT) spectrum analyzer scripted in LabVIEW were used.

Numerical methods

Finite element solver COMSOL Multiphysics 5.2a with the acoustic module was used to perform full-wave simulation. In the acoustic propagation wave equation, the speed of sound was set to 343.2 m/s and the density of air was set to 1.225 kg/m 3 . Other dimensional parameters of the structure are the same as the fabricated parameters.

TBM is used to fit the band diagrams of the dimerized and undimerized structures with the first-principles COMSOL solution. For the undimerized band structure with X-W line degeneracy, the onsite frequency is fitted as $\omega_0=8584$ Hz and $\kappa=\gamma=12.8$ Hz. For the dimerized band structure with X-W line broken degeneracy, $\omega_0=8470$ Hz and $\kappa=12.8$ Hz, $\gamma=115$ Hz (κ and γ are flipped for the shrunken case). These numbers were used to extract the bulk polarization of the expanded and shrunken cases.

Data analysis

Normalized response spectra measurement

The speaker was placed at the bottom port and the microphone was placed at the top port of the same site. The frequency generator was used to run a sweep from 7600 to 8800 Hz in 20-Hz intervals with a dwell time of 0.5 s, while the FFT spectrum analyzer obtained the amplitude responses $\varphi(\omega)$ at each frequency. Field distributions $\varphi_j(\omega)$ are obtained by repeating this process for each site j. Once each amplitude response was obtained for each of the 80 individual sites, we separate the response of the bulk, surface, edge, and corner sites depending on which mode dominates at that site by using a filter function (as shown in the inset for Fig. 3B) to obtain the spectra for each different type of mode. We obtained the average power spectrum $P_a(\omega) = \sum_j |\Phi_j(\omega)|^2/N$ for each colored region, where N is the number of resonators within that region, and then normalized the spectra with $P_n(\omega) = P_a(\omega)/\sum_\omega P_a(\omega)$. For the field profiles excited by a single frequency, the speaker was fixed at the port of the

site of interest, and the microphone was placed over each site of the lattice to measure the magnitude response at the desired frequency (shown in Fig. 3B). The same method was used for the shrunken lattice as shown in fig. S2.

Spatial distribution measurement

The speaker was placed at the bottom port of a single site, while the microphone was placed at the top port of any other individual site. Depending on which mode we wanted to observe, we set the frequency generator to a single frequency: I, II, III, or IV from Fig. 3B. While keeping the speaker in place, we obtained the amplitude response at each site in the lattice by placing the microphone at the top port of the site. If there was no measurable amplitude response above background noise level at a certain site, then we considered the response "zero" and colored it gray in Fig. 3C.

SUPPLEMENTARY MATERIALS

Supplementary material for this article is available at http://advances.sciencemag.org/cgi/content/full/6/13/eaay4166/DC1

Section S1. Eigenvalues and eigenstates of the pyrochlore lattice from TBM Section S2. Critical coupling ratio when zero-energy corner state intersects the bulk continuum

Section S3. Generalized chiral symmetry for crystal with four sublattices Section S4. Trivial insulating phase

Fig. S1. Condition for the upper dispersive mode to approach the zero-energy line.

Fig. S2. Experimental demonstration of the trivial phase.

REFERENCES AND NOTES

- R. Süsstrunk, S. D. Huber, Classification of topological phonons in linear mechanical metamaterials. Proc. Natl. Acad. Sci. U.S.A. 113, E4767–E4775 (2016).
- C. L. Kane, T. C. Lubensky, Topological boundary modes in isostatic lattices. Nat. Phys. 10, 39–45 (2014).
- N. P. Mitchell, L. M. Nash, D. Hexner, A. M. Turner, W. T. M. Irvine, Amorphous topological insulators constructed from random point sets. *Nat. Phys.* 14, 380–385 (2018).
- K. Bertoldi, V. Vitelli, J. Christensen, M. van Hecke, Flexible mechanical metamaterials. Nat. Rev. Mater. 2, 17066 (2017).
- Z. Yang, F. Gao, X. Shi, X. Lin, Z. Gao, Y. Chong, B. Zhang, Topological acoustics. Phys. Rev. Lett. 114, 114301 (2015).
- A. B. Khanikaev, R. Fleury, S. H. Mousavi, A. Alù, Topologically robust sound propagation in an angular-momentum-biased graphene-like resonator lattice. *Nat. Commun.* 6, 8260 (2015)
- R. Fleury, A. B. Khanikaev, A. Alù, Floquet topological insulators for sound. *Nat. Commun.* 7, 11744 (2016).
- 8. S. D. Huber, Topological mechanics. Nat. Phys. 12, 621–623 (2016).
- P. Wang, L. Lu, K. Bertoldi, Topological phononic crystals with one-way elastic edge waves. *Phys. Rev. Lett.* 115, 104302 (2015).
- V. Peano, C. Brendel, M. Schmidt, F. Marquardt, Topological phases of sound and light. Phys. Rev. X 5, 031011 (2015).
- L. M. Nash, D. Kleckner, A. Read, V. Vitelli, A. M. Turner, W. T. M. Irvine, Topological mechanics of gyroscopic metamaterials. *Proc. Natl. Acad. Sci. U.S.A.* 112, 14495–14500 (2015).
- M. Xiao, G. Ma, Z. Yang, P. Sheng, Z. Q. Zhang, C. T. Chan, Geometric phase and band inversion in periodic acoustic systems. *Nat. Phys.* 11, 240–244 (2015).
- R. Süsstrunk, S. D. Huber, PHYSICS. Observation of phononic helical edge states in a mechanical topological insulator. Science 349, 47–50 (2015).
- C. He, X. Ni, H. Ge, X.-C. Sun, Y.-B. Chen, M.-H. Lu, X.-P. Liu, Y.-F. Chen, Acoustic topological insulator and robust one-way sound transport. *Nat. Phys.* 12, 1124–1129 (2016).
- M. Miniaci, R. K. Pal, B. Morvan, M. Ruzzene, Experimental observation of topologically protected helical edge modes in patterned elastic plates. Phys. Rev. X 8, 031074 (2018).
- S. H. Mousavi, A. B. Khanikaev, Z. Wang, Topologically protected elastic waves in phononic metamaterials. Nat. Commun. 6, 8682 (2015).
- X. Ni, M. A. Gorlach, A. Alu, A. B. Khanikaev, Topological edge states in acoustic Kagome lattices. New J. Phys. 19, 055002 (2017).
- S. Yves, R. Fleury, F. Lemoult, M. Fink, G. Lerosey, Topological acoustic polaritons: Robust sound manipulation at the subwavelength scale. New J. Phys. 19, 075003 (2017).
- H. Xue, Y. Yang, F. Gao, Y. Chong, B. Zhang, Acoustic higher-order topological insulator on a Kagome lattice. *Nat. Mater.* 18. 108–112 (2019).
- X. Ni, M. Weiner, A. Alu, A. B. Khanikaev, Observation of higher-order topological acoustic states protected by generalized chiral symmetry. *Nat. Mater.* 18, 113–120 (2019).

SCIENCE ADVANCES | RESEARCH ARTICLE

- H. Ge, X. Ni, Y. Tian, S. K. Gupta, M.-H. Lu, X. Lin, W.-D. Huang, C. T. Chan, Y.-F. Chen, Experimental observation of acoustic weyl points and topological surface states. *Phys. Rev. Appl.* 10, 014017 (2018).
- F. Li, X. Q. Huang, J. Y. Lu, J. H. Ma, Z. Y. Liu, Weyl points and Fermi arcs in a chiral phononic crystal. *Nat. Phys.* 14, 30–34 (2018).
- M. Xiao, W.-J. Chen, W.-Y. He, C. T. Chan, Synthetic gauge flux and Weyl points in acoustic systems. Nat. Phys. 11, 920–924 (2015).
- C. He, S.-Y. Yu, H. Ge, H. Wang, Y. Tian, H. Zhang, X.-C. Sun, Y. B. Chen, J. Zhou, M.-H. Lu, Y.-F. Chen, Three-dimensional topological acoustic crystals with pseudospin-valley coupled saddle surface states. *Nat. Commun.* 9, 4555 (2018).
- M. Serra-Garcia, V. Peri, R. Süsstrunk, O. R. Bilal, T. Larsen, L. G. Villanueva, S. D. Huber, Observation of a phononic quadrupole topological insulator. *Nature* 555, 342–345 (2018).
- W. A. Benalcazar, B. A. Bernevig, T. L. Hughes, Electric multipole moments, topological multipole moment pumping, and chiral hinge states in crystalline insulators. *Phys. Rev. B* 96, 245115 (2017).
- W. A. Benalcazar, B. A. Bernevig, T. L. Hughes, Quantized electric multipole insulators. Science 357, 61–66 (2017).
- M. Ezawa, Higher-order topological insulators and semimetals on the breathing kagome and pyrochlore lattices. Phys. Rev. Lett. 120, 026801 (2018).
- F. Zangeneh-Nejad, R. Fleury, Topological fano resonances. Phys. Rev. Lett. 122, 014301 (2019).
- M. Ezawa, Minimal models for Wannier-type higher-order topological insulators and phosphorene. Phys. Rev. B 98, 045125 (2018).

 R. D. Kingsmith, D. Vanderbilt, Theory of polarization of crystalline solids. *Phys. Rev. B* 47, 1651–1654 (1993).

Acknowledgments: M.W. acknowledges the guidance of B. Hahn for the preparation of 3D graphics. Funding: The work was supported by the DARPA Nascent program and by the National Science Foundation (grants CMMI-1537294, EFRI-1641069, Waterman award, and DMR-1809915). Research was carried out, in part, at the Center for Functional Nanomaterials, Brookhaven National Laboratory, which is supported by the U.S. Department of Energy, Office of Basic Energy Sciences, under contract no. DE-SC0012704. Author contributions: A.B.K., A.A., and M.W. initiated the research. M.W., X.N., and M.L. developed the theoretical model. M.W. performed numerical simulations and designed the structure. M.W. designed and carried out the experiment. M.W. and X.N. performed the data analysis. A.B.K. and A.A. supervised the research. All the coauthors contributed to the writing of the main text. Competing interests: The authors declare that they have no competing interests. Data and materials availability: All data needed to evaluate the conclusions in the paper are present in the paper and/or the Supplementary Materials. Additional data related to this paper may be requested from the authors.

Submitted 17 June 2019 Accepted 2 January 2020 Published 27 March 2020 10.1126/sciadv.aay4166

Citation: M. Weiner, X. Ni, M. Li, A. Alù, A. B. Khanikaev, Demonstration of a third-order hierarchy of topological states in a three-dimensional acoustic metamaterial. Sci. Adv. 6, eaay4166 (2020).